Probing the Active Site of Human Manganese Superoxide Dismutase: The Role of Glutamine 143[†,‡]

Yunsheng Hsieh,[§] Yue Guan,[||] Chingkuang Tu,[§] Peter J. Bratt,[⊥] Alexander Angerhofer,[⊥] James R. Lepock,[○] Michael J. Hickey,[||] John A. Tainer,[||] Harry S. Nick,[▽] and David N. Silverman*[,§]

Departments of Pharmacology and Therapeutics, Biochemistry and Molecular Biology, and Chemistry, University of Florida, Gainesville, Florida 32610, Department of Molecular Biology, The Scripps Research Institute, 10550 North Torrey Pines Road, La Jolla, California 92037, and Department of Physics, University of Waterloo, Waterloo, Ontario N2L3G1, Canada

Received September 26, 1997; Revised Manuscript Received January 26, 1998

ABSTRACT: Structural and biochemical characterization of the nonliganding residue glutamine 143 near the manganese of human Mn superoxide dismutase (hMnSOD), a homotetramer of 22 kDa, reveals a functional role for this residue. In the wild-type protein, the side-chain amide group of Gln 143 is about 5 Å from the metal and is hydrogen-bonded to Tyr 34, which is a second prominent side chain adjacent to the metal. We have prepared the site-specific mutant of hMnSOD with the conservative replacement of Gln 143 → Asn (Q143N). The crystal structure of Q143N shows that the side-chain amide nitrogen of residue 143 is 1.7 Å more distant from the manganese than in the wild-type enzyme. The Tyr 34 side-chain hydroxyl in Q143N is also moved to become 0.6 Å more distant from the metal due to an additional water molecule. Differential scanning calorimetry showed that Q143N is slightly more stable than the wild-type enzyme with T_m for the main unfolding transition increased by 2 °C to 90.7 °C. Pulse radiolysis and stopped-flow spectrophotometry reveal that unlike wild-type hMnSOD, which is strongly inhibited by peroxide, Q143N MnSOD exhibits no product inhibition even at concentrations of $O_2^{\bullet -}$ in the millimolar range, and its catalysis follows Michaelis kinetics with no evidence of cooperativity. However, the overall catalytic activity of this mutant was decreased 2−3 orders of magnitude compared with the wild-type MnSOD, which can account for its lack of product inhibition. Q143N MnSOD lacked the visible absorption spectrum typical of wild-type Mn(III)SOD. Also, unlike the wild-type Mn(III)-SOD, which is electron paramagnetic resonance (EPR) silent, Q143N MnSOD has a complex EPR spectrum with many resonances in the region below 2250 G. We conclude that the Gln 143 → Asn mutation has increased the reduction potential of manganese to stabilize Mn(II), indicating that Gln 143 has a substantial role in maintaining a reduction potential favorable for the oxidation and reduction cycles in the catalytic disproportionation of superoxide. A solvent hydrogen isotope effect near 2 for k_{cat} in catalysis by Q143N hMnSOD indicates rate-contributing proton transfers to form product hydroperoxide anion or hydrogen peroxide. The data demonstrate a prominent role for Gln 143 in maintaining the microenvironment of the manganese and in efficient catalysis of superoxide dismutation to oxygen and hydrogen peroxide.

Crystal structures of human Mn superoxide dismutase (hMnSOD)[1] have been determined at 2.2 Å resolution (*1*) and 3 Å resolution (*2*); these are very similar to those of the bacterial MnSODs from *Bacillus stearothermophilus* at 2.4 Å resolution (*3*) and from *Thermus thermophilus* at 1.8 Å resolution (*4*). The structure at 2.9 Å resolution of FeSOD from *Pseudomonas ovalis* (*5*) also has a very similar structure including the same ligands to and approximate geometry about the metal. However, none of these enzymes are structurally related to Cu/ZnSOD. In hMnSOD, the geometry about the metal is trigonal bipyramidal with three histidine ligands (His 26, 74, and 163), one aspartate (Asp 159), and a water molecule or hydroxide as a fifth ligand (*1*). The hMnSOD is a homotetramer (*1*, *6*, *7*), but it is more compact than the reported bacterial MnSODs as seen by the shorter distances between metals (*1*); these are due in large part to differences in the interfacial regions between subunits. In addition, the tetrameric structure of hMnSOD forms a ring of positive electrostatic charge surrounding an active site;

[†] This work was supported by the Office of Research, Technology, and Graduate Education, University of Florida, and by grants from the National Institutes of Health GM54903 (to D.N.S.), GM48495 (to J.A.T.), HL39593 (to H.S.N.), and F32CA69107 (to Y.G.) and from the National Science Foundation DMR9601864 (to A.A.).

[‡] Atomic coordinates have been deposited in the Brookhaven Protein Data Bank under accession code 1QNM.

* Address correspondence to this author at Box 100267 Health Center, University of Florida, Gainesville, FL 32610-0267. Phone (352) 392-3556; Fax (352) 392-9696; e-mail silvrmn@nervm.nerdc.ufl.edu.

[§] Department of Pharmacology and Therapeutics, University of Florida.

[||] The Scripps Research Institute.

[⊥] Department of Chemistry, University of Florida.

[○] University of Waterloo.

[▽] Department of Biochemistry and Molecular Biology, University of Florida.

[1] Abbreviations: MnSOD, manganese superoxide dismutase; hMnSOD, human manganese superoxide dismutase; Q143N MnSOD, mutant of manganese superoxide dismutase containing the replacement glutamine 143 → asparagine; Y34F MnSOD, mutant of manganese superoxide dismutase containing the replacement tyrosine 34 → phenylalanine; DSC, differential scanning calorimetry.

S0006-2960(97)02395-7 CCC: $15.00
Published on Web 03/19/1998

this is suggested to enhance attraction of substrate (*1*), as has been shown to occur in Cu/ZnSOD and mutants (*8*).

It is now widely accepted that superoxide dismutases carry out catalysis through a redox process in which the metal cycles between oxidized and reduced states (*9*):

$$Mn^{3+} + O_2^{\bullet -} \underset{k_{-1}}{\overset{k_1}{\rightleftharpoons}} [Mn^{3+}-O_2^{\bullet -}] \xrightarrow{k_2} Mn^{2+} + O_2 \quad (1)$$

$$Mn^{2+} + O_2^{\bullet -} \underset{k_{-3}}{\overset{k_3}{\rightleftharpoons}} [Mn^{2+}-O_2^{\bullet -}] + 2H^+ \xrightarrow{k_4} Mn^{3+} + H_2O_2 \quad (2)$$

Initial studies of the MnSOD from *B. stearothermophilus* determined that its catalysis is complicated by the presence of an inactive form of the enzyme that can interconvert to an active form, but these studies did not designate the nature of the inactive form (*10*, *11*). Steady-state constants for catalysis by MnSOD from *T. thermophilus* were obtained by Bull et al. (*12*) from stopped-flow experiments, and for the human MnSOD using both stopped-flow and pulse radiolysis (*6*); in both, the rapid emergence of the inactive form of the enzyme was quantitated. Bull et al. (*12*) observed the inactive form spectrophotometrically and suggested that it results from oxidative addition of $O_2^{\bullet -}$ to the Mn(II) form of the enzyme, resulting in a side-on peroxo complex of Mn(III).

In this study we have investigated the function of an active-site residue, Gln 143, which is close to the active-site manganese but is not a ligand of this metal. Glutamine 143 is conserved in the majority of the known MnSODs and in some bacterial forms of the enzyme (*13*). The adjacent residue Tyr 34 is conserved in all of the MnSODs reported to date and in the FeSODs as well. Glutamine 143 is part of an extensive hydrogen-bond network that includes Tyr 34 and the metal−ligand cluster and may connect the properties of this tyrosine to catalysis at the metal. The amide group of Gln 143 (Nϵ2) is 4.6 Å from the manganese and 2.7 Å from the hydroxyl group of Tyr 34 to which it is hydrogen-bonded (*1*). In the complex of azide with Mn(III)SOD from *T. thermophilus*, the azide is a ligand of the metal, forming a hydrogen bond to the hydroxyl group of Tyr 34 (*14*).

We have replaced Gln 143 with Asn and measured the catalytic properties of the resulting mutant (Q143N hMnSOD). This replacement decreased the catalytic rate of superoxide decay by at least 2 orders of magnitude. Moreover, the reduction potential of manganese in Q143N hMnSOD appears to be shifted to a more positive value compared with the wild type; electron paramagnetic resonance (EPR) evidence as well as visible absorption spectra demonstrate that this mutant favors Mn(II) in the resting state whereas the wild-type MnSOD is predominantly in the Mn(III) state. The crystal structure of the mutant Q143N hMnSOD shows that an additional water molecule fills the cavity left by the replacement of Gln 143 and that the adjacent residue Tyr 34 has been pushed away by the newly introduced water molecule and is no longer able to maintain the direct hydrogen bonding with Asn 143. The new water forms three hydrogen bonds that link the ligand H_2O/OH^-, Asn 143, and Tyr 34 and thus may stabilize the mutant structure. These features are discussed in terms of the new information they provide on the catalytic pathway.

MATERIALS AND METHODS

PCR-Based Site-Directed Mutagenesis. The oligonucleotides GCATATGAAGCACAGCCTCC and GGAGATCTCAGCATAACGATC were used as primers for PCR to amplify the hMnSOD cDNA [cDNA sequence reported by Beck et al. (*15*)]. The plasmid pHMNSOD4 (ATCC 59947), which encodes hMnSOD, was subcloned into the TA cloning vector pCRII (Invitrogen Corp.). Four primers were designed and used for PCR-based site-directed mutagenesis to create the mutant Q143N hMnSOD. First we designed a pair of oligonucleotides, primers 1 (5′ GCAGCTTACTGTATTCTGCAG 3′) and 2 (5′ CCTTTAAACACAGCCTCCCCG 3′), which through PCR recreate the entire MnSOD coding region flanking the mutation. In addition we prepared two oligonucleotides, designated as primers 3 (5′ GCTTGTCCAAATAACGATCCACTGC 3′) and 4 (5′ AGTGGATCGTTATTTGGACAAGC 3′), whose sequences were complementary to each other and contained the mutation of interest. Two separate PCR reactions were used to amplify the 5′ portion (primers 1 and 4) and 3′ portion (primers 3 and 2) of the MnSOD cDNA. The PCR products from these two reactions were purified by electroelution and used as template DNA for the second round of PCR using primers 1 and 2. The Q143N hMnSOD PCR product was cloned into the TA cloning vector (pCRII) and subsequently subcloned into the expression vector pTrc 99A (Pharmacia Corp.). The subcloning was accomplished by using the restriction sites, *Dra*I and *Pst*I, incorporated into primers 1 and 2, respectively. The *Dra*I site, which corresponds to the N-terminal portion of the protein, was annealed to the *Nco*I site in pTrc 99A, recreating an ATG codon, whereas the C-terminal end of the cDNA was annealed to the *Pst*I site of the vector. The mutation, along with the remainder of the coding sequence, was verified by DNA sequencing. This construct expressed hMnSOD in the mutant *SodA*$^-$/*SodB*$^-$ *Escherichia coli* (strain QC 774) as a mature protein tagged with an extra Met at the amino terminus. Culture conditions included additional supplementation by 5 mM $MnCl_2$. Yields of MnSOD mutant protein were on average 50 mg of protein/50 g of bacterial pellet.

Purification of Human MnSOD. The mutant Q143N hMnSOD was purified from *E. coli* using a combination of heat treatment (60 °C) and ion-exchange chromatography (DE52 and CM52) according to the procedures of Beck et al. (*16*). The purity of the resulting samples was determined on SDS−polyacrylamide gels, which showed one intense band. The purified enzyme was dialyzed extensively against EDTA and a portion of the resulting protein was digested with nitric acid for manganese analysis by atomic absorption spectrometry (Perkin-Elmer 5100PC). These measurements were used to determine the concentration of enzyme.

Crystallization and Diffraction Data Collection. Crystallization of human Q143N MnSOD was difficult and required conditions different than those for the native and other mutants of human MnSOD. Moreover, crystals grown under most conditions were mosaic and diffracted poorly, suggesting possible conformational variation because the Gln 143 site is not surface-exposed. Crystals grown from solutions

containing ammonium sulfate, poly(ethylene glycol) (PEG) 4000, and PEG 400 did not diffract well. Diffraction-quality crystals of the Q143N mutant were grown at room temperature using the hanging drop and sitting drop methods. The best crystals grew from solutions consisting of 20 mg/mL protein buffered in 40 mM sodium acetate, pH 4.6, 20% poly(ethylene glycol) 2000 monomethyl ether (MEPEG 2000), 200 mM ammonium sulfate, and 0.8% 1,2,3-heptanetriol. Crystals were isomorphous to the native crystals with one dimer per asymmetric unit in space group $P2_12_12$ with unit cell dimensions of $a = 75.5$ Å, $b = 78.6$ Å, and $c = 67.7$ Å.

A crystal was flash-cooled to −190 °C using an Area Detector Systems Corp. cryogenic device. A complete data set to 2.3 Å resolution was collected from this one cooled crystal using a MAR image plate detector and SRA generator at The Scripps Research Institute and processed using the DENZO program suite (*17*). A total of 18 015 unique reflections (55 987 total measurements) were collected. The R_{sym} on intensities was 9.2%. The data are 96.4% complete from 99 to 2.3 Å resolution [94.3% when a signal-to-noise ratio ($F/\sigma F$) greater than 3 is applied] and 80% complete for the 2.4−2.3 Å resolution shell (75.2% complete with a 3σ cutoff).

Crystallographic Refinement. The initial atomic model was generated by replacing the Gln 143 side chain with Asn in the native model using Xfit (*18*), which was then refined with X-PLOR (*19*). After simulated annealing refinement, the *R* value dropped to 28%. The anisotropic temperature factor refinement and bulk solvent corrections with X-PLOR (*20*) further lowered the *R*-factor to 23%. σ_A-weighted $2F_o-F_c$ and F_o-F_c electron density maps (*21*) were displayed and fitted using Xfit. After many rounds of refinement and model refitting, the model converged to an *R* value of 0.198 (R_{free} of 0.294). The manganese ion was completely unrestrained during the final round of refinement to remove any force field bias. The final model consists of two 198-residue Q143N MnSOD subunits, 220 water molecules, and two trigonal bipyramidal coordinated Mn ions. The overall deviations from ideal geometry were 0.011 Å for bond distances and 1.5° for bond angles. The average temperature factor *B*-value is 38.6 Å^2 for protein atoms. The Ramachandran plot (*22*) shows that 196 out of 198 residues are in the energy allowable regions. Two outliers are Asn 142 and Lys 170, being at the second position of type II′ turns. Atomic coordinates have been deposited in the Brookhaven Protein Data Bank (*23*) with accession code 1QNM.

Differential Scanning Calorimetry. Microcal-2 and a CSC Nano high-sensitivity differential scanning calorimeters were used to obtain all denaturation profiles. Similar profiles were obtained from both calorimeters. Human MnSOD and mutant at 1.0−3.0 mg/mL in 2 mM potassium phosphate buffer (pH 7.8) were deaerated under mild vacuum for 5 min and immediately scanned at a rate of temperature increase of 1 °C/min. The baseline and change in specific heat (ΔC_p) upon denaturation were corrected as previously described (*24*). The peaks of the differential scanning calorimetry profile were deconvoluted assuming a reversible, non-two-state model (*25*) using the software package ORIGIN (Microcal, Inc.). ΔH, ΔS, and T_m, defined as the temperature of half-completion, for each transition were obtained from the best fits.

Pulse Radiolysis. Experiments were carried out at the Center for Fast Kinetics Research at the University of Texas at Austin using a 4-Mev van der Graaff accelerator. A single high-dose electron pulse was used to generate superoxide radical anions from oxygen in aqueous solutions containing 10 mM sodium formate as hydroxyl radical scavenger (*26*) and 50 μM EDTA in addition to buffer and enzyme. All pulse radiolysis experiments were carried out at 20 °C. The dismutation of $O_2^{\bullet -}$ was followed spectrophotometrically from its absorbance at 250 nm [$\epsilon = 2000$ M^{-1} cm^{-1} (*27*)] with a path length of 2.5 cm. Progress curves for each set of 6−9 experiments were averaged. Exposure to ultraviolet radiation was minimized by opening a mechanical shutter a fraction of a second before each pulse.

Stopped-Flow Spectrophotometry. Experiments are based on the stabilization of KO_2 in aprotic solvent and the subsequent large dilution of this solution by an aqueous solution of enzyme in a stopped-flow apparatus, as described by McClune and Fee (*28*). KO_2 was dissolved in a mixture of dimethyl sulfoxide and *N*,*N*-dimethyl sulfoxide (2:1 by volume; Aldrich, spectrophotometric grade) with solubility of KO_2 enhanced with 18-crown-6 ether (*29*). The stopped-flow spectrophotometer (Kinetic Instruments, Ann Arbor, MI) was capable of efficient mixing of this solution with an aqueous solution of enzyme in buffer with a dead time between 1.5 and 2.0 ms. One drive syringe (capacity 50 μL) contained the aprotic solution of $O_2^{\bullet -}$; this was diluted 50-fold by the contents of a second syringe (capacity 2.5 mL) that contained enzyme, EDTA, and buffer. The decay of superoxide in initial velocity experiments and progress curves was monitored by its absorption at 250−300 nm. Stopped-flow experiments reported here were carried out at 5 °C. Four or more kinetic traces were averaged to reduce noise. Steady-state parameters were obtained by least-squares analysis of such data [Enzfitter (*30*)].

EPR Spectroscopy. EPR spectra were recorded at X-band frequencies on a Bruker ESP300E instrument equipped with a variable-temperature liquid helium cooled cryogenic sample dewar (Oxford Instruments). Samples (∼200 μL) were studied in standard quartz EPR tubes and were not deoxygenated.

RESULTS

Catalysis and Spectroscopy. Previous studies using stopped-flow (*10*−*12*) and pulse radiolysis (*6*) determined that bacterial and human MnSOD demonstrate a biphasic pattern in the decay of $O_2^{\bullet -}$ under conditions for which the ratio $[O_2^{\bullet -}]/[E]$ is greater than approximately 10. This biphasic pattern is an initial burst of catalysis followed by a much slower zero-order rate of the disproportionation of superoxide representing an inhibited phase. We used pulse radiolysis to measure the rapid initial burst of activity with wild-type hMnSOD before the phase of inhibition began, which was 1 or 2 ms after initiating catalysis under the conditions of Figure 1 (top). This region was not observable by stopped-flow due to the mixing times in the instrument. When observed by pulse radiolysis and stopped-flow under similar conditions, catalysis by Q143N MnSOD showed no inhibited region up to $[O_2^{\bullet -}]/[E]$ as great as 50 and was described throughout its entire decay by a single first-order process using up to 1.0 mM superoxide (shown under conditions of

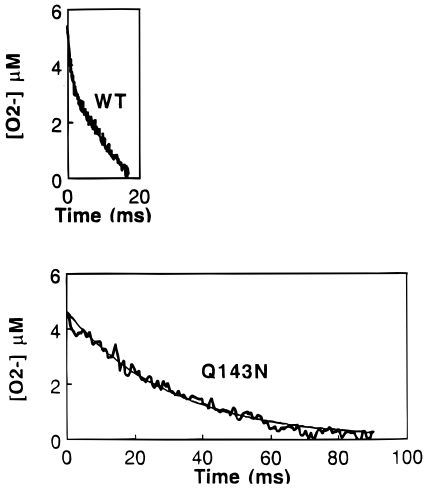

FIGURE 1: Comparison of superoxide decay catalyzed by (top) wild-type human MnSOD and (bottom) Q143N human MnSOD as determined by pulse radiolysis. Data show the decrease in superoxide as determined from its absorbance at 250 nm ($\epsilon = 2000$ M^{-1} cm^{-1}). The solutions contained 0.5 μM wild-type MnSOD or 35 μM Q143N MnSOD and 50 μM EDTA, 10 mM sodium formate, and 2.0 mM sodium pyrophosphate at pH 9.6 and 20 °C. The solid line for Q143N MnSOD is a least-squares fit to a first-order process corresponding to $k_{cat}/K_m = 1 \times 10^6$ M^{-1} s^{-1}. The uncatalyzed dismutation rate was measured under these conditions and showed a change in $O_2^{\bullet -}$ concentration consistent with a bimolecular dismutation rate constant of 1800 M^{-1} s^{-1}.

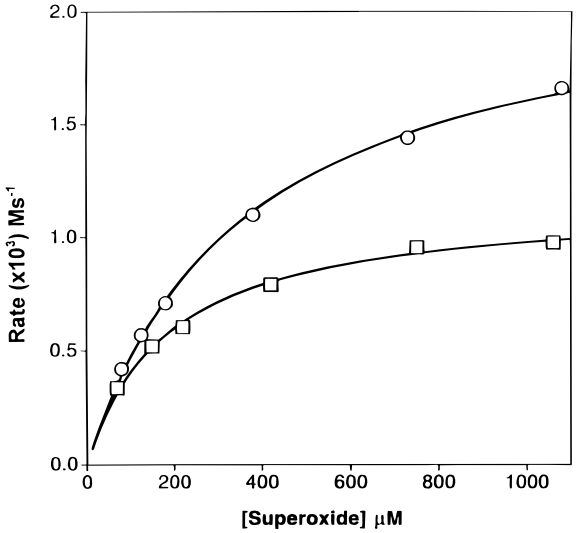

FIGURE 2: Rate of superoxide decay in H_2O (○) and in D_2O (□) catalyzed by Q143N human manganese superoxide dismutase measured by stopped-flow spectrophotometry. The concentration of Q143N MnSOD was 7.3 μM in a solution containing 50 mM glycine buffer and 1 mM EDTA at pH 9.4 and 5 °C. The solid line for H_2O is a least-squares fit of the Michaelis−Menten equation to the data resulting in $k_{cat} = 300$ s^{-1} and $k_{cat}/K_m = 8.2 \times 10^5$ M^{-1} s^{-1}; for D_2O the values are $k_{cat} = 160$ s^{-1} and $k_{cat}/K_m = 8.5 \times 10^5$ M^{-1} s^{-1}.

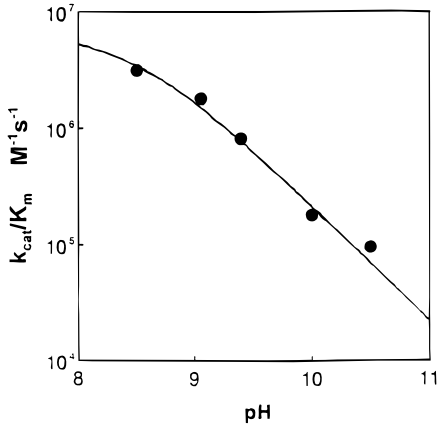

FIGURE 3: Steady-state constant k_{cat}/K_m for the decay of superoxide catalyzed by Q143N human manganese superoxide dismutase as a function of pH as determined by stopped-flow spectrophotometry at 5 °C. A concentration of 50 mM of one of the following buffers was used: Taps (at pH 8.5); Ches (pH 9.0); glycine (pH 9.4); Caps (pH 10 and 10.5). The standard error in individual points is less than 10%. The solid line is a least-squares fit with $pK_a = 8.5 \pm 0.3$ and a maximal value of $k_{cat}/K_m = (7 \pm 3) \times 10^6$ M^{-1} s^{-1}.

low substrate concentration in Figure 1, bottom). The apparent lack of inhibition for Q143N MnSOD, even under a wide range of conditions, allowed us to utilize stopped-flow spectrophotometry to a greater extent than for wild type since the uninhibited catalysis was measurable after the instrument's dead time of 1.5−2.0 ms.

The initial velocities for the decay of $O_2^{\bullet -}$ catalyzed by Q143N MnSOD were adequately described by simple Michaelis−Menten kinetics; typical data are shown in Figure 2. The pH profile for k_{cat}/K_m over the range of pH 8.5−10.5 included a region of negative slope near unity, suggesting a dependence of the catalysis on the protonated form of a single group with pK_a near or below 8.5 (Figure 3). The value of k_{cat}/K_m observed at pH 9.4 was 7×10^5 M^{-1} s^{-1} at 5 °C, about 3 orders of magnitude less than k_{cat}/K_m for wild-type hMnSOD at pH 9.6, which is 8×10^8 M^{-1} s^{-1} (*6*; these data reported for 20 °C).

The pH dependence of k_{cat} for the decay of $O_2^{\bullet -}$ catalyzed by Q143N MnSOD suggested a pK_a near 10 with a maximal value near 300 s^{-1} (Figure 4). This is also much less than the value of $k_{cat} = 4 \times 10^4$ s^{-1} observed for the wild-type hMnSOD at pH 9.6 (*6*). The solvent hydrogen isotope effects on the steady-state parameters of the reaction catalyzed by Q143N MnSOD were measured at pH 9.4 (typical data in Figure 2): $(k_{cat})_{H_2O}/(k_{cat})_{D_2O} = 1.9 \pm 0.2$; $(k_{cat}/K_m)_{H_2O}/(k_{cat}/K_m)_{D_2O} = 1.0 \pm 0.1$. Identical values were obtained when these isotope effects were measured at pH 10.0. This solvent hydrogen isotope effect on k_{cat} is consistent with a rate-contributing proton transfer to the active site during maximal turnover. We did not observe any enhancement of catalysis upon increasing the concentration of the following buffers from 2 to 100 mM: glycine (at pH 9.6) and ethanolamine (at pH 10.0).

Two other properties of Q143N hMnSOD were observed to be different from the wild-type enzyme. Whereas the wild-type hMnSOD was observed to have a broad visible absorption spectrum with a maximum at 480 nm assigned to Mn(III) (*6*), which is consistent with the MnSOD from *E. coli* (*31*), the mutant Q143N MnSOD had no detectable visible absorption. Atomic absorption verified that Q143N MnSOD contained manganese with a molar ratio of manganese to enzyme subunit near 0.7 as observed with the wild-type enzyme (*6*, *12*). Second, whereas the EPR of wild-type MnSOD showed little or no indication of Mn^{2+} resonances, the X-band EPR spectrum of Q143N MnSOD at 4 K (Figure 5) showed a spectrum at 1000−2000 G with hyperfine splitting suggestive of the spin $^5/_2$ of $^{55}Mn^{2+}$. The source of the weak and poorly resolved multiplet near 3000 G is uncertain.

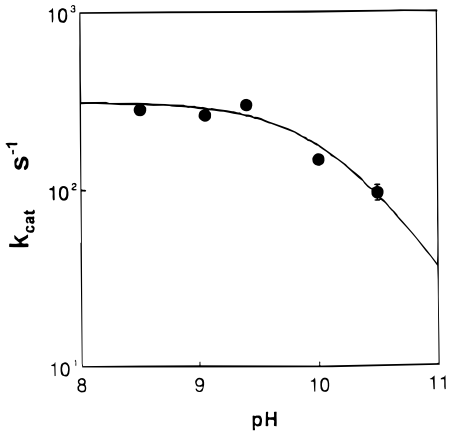

FIGURE 4: Steady-state constant k_{cat} for the dismutation of superoxide catalyzed by Q143N human manganese superoxide dismutase as a function of pH as determined by stopped-flow spectrophotometry at 5 °C. Conditions are as in Figure 3. The standard error in individual points is less than 10%. The solid line is a least-squares fit with pK_a = 10.1 ± 0.2 and a maximal value of k_{cat} = 310 ± 30.

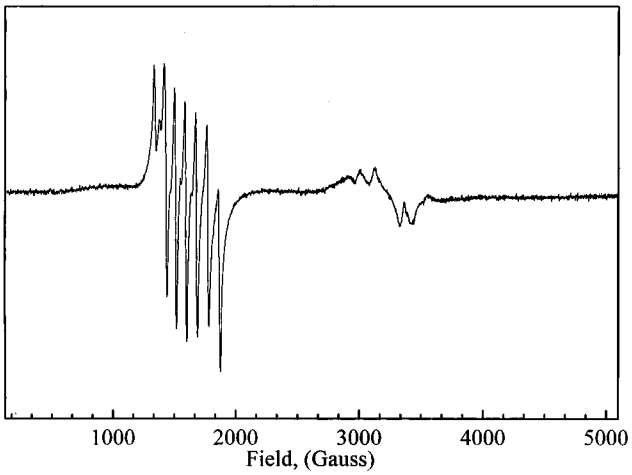

FIGURE 5: X-band EPR spectrum of Q143N human manganese superoxide dismutase (1.8 mM) at 4 K in solution containing 20 mM potassium phosphate buffer at pH 7.8. Instrumental parameters: microwave frequency, 9.46 GHz; microwave power, 0.2 mW; modulation amplitude, 7.86 G; modulation frequency, 12.50 kHz.

Table 1: Thermodynamic Parameters for Reversible Unfolding of MnSOD

enzyme	component	T_m (°C)	ΔH^a (kcal/mol)	$\Delta\Delta G^b$ (kcal/mol)	$\Delta\Delta G^{*c}$ (kcal/mol)
native	B	70	142	0	0
native	C	88.9	90.6	0	0
Q143N	A	57.4	100		
Q143N	B	85.3	78.3	3.35	2.79
Q143N	C	90.7	157	0.8	0.06

[a] ΔH and ΔG are given per mole of tetramer. [b] $\Delta\Delta G$ is ΔG of the mutant calculated at the appropriate T_m of the native, assuming constant ΔH (ΔC_p = 0). [c] $\Delta\Delta G^*$ was calculated assuming ΔC_p = 0.12 cal/g.

Thermal Stability. The thermal stability of Q143N hMnSOD was determined by differential scanning calorimetry (DSC). Three peaks were resolvable for Q143N MnSOD, a very weak one (designated A in Table 1) with $T_m \sim 57$ °C, a poorly resolved peak designated B with $T_m \sim 85$ °C, and a larger one (designated C) with $T_m \sim 91$ °C. This notation for labeling the transitions was chosen to correspond to that used previously for native and I58T MnSOD (*24*). Transition C is the main unfolding transition of the enzyme. Q143N is slightly more stable than native MnSOD, with increases of 15 °C in T_m (B) and 2 °C in T_m (C). The identity of transitions A and B are unknown; however, the T_m of transition B corresponds to the thermal inactivation temperature (*24*). Thus this transition, which occurs with a relatively small absorption of heat, results in an inactive enzyme. Transition A is not observed in native MnSOD, appears to have multiple components in I58T and Y34F MnSOD (*32*), and is extremely weak and nearly undetectable in Q143N MnSOD. It has no effect on activity (*24*). Transitions B and C are less well resolved since the T_ms differ by only 5.4 °C compared to 19 °C in native MnSOD (*24*).

The estimated stabilization of the mutant compared to native enzyme, given as $\Delta\Delta G$, was calculated from the thermodynamic parameters ΔH, ΔS, and T_m (Table 1). A reversible analysis of an apparently irreversible process is appropriate, and is commonly done, if there is little accumulation of the irreversibly denatured species during that part of the DSC scan used for analysis (*25*). Irreversible species will accumulate near the high-temperature end of each transition; therefore, to minimize errors in determining ΔH and ΔS, the high-temperature end was excluded in the reversible curve-fitting (*33*). As expected for an irreversible transition, the high-temperature end of the DSC profiles are not fit well with the reversible model because of the sharp drop in the C_p above the T_m of peak C, which is a consequence of irreversibility (*33*). To reduce this fitting problem, peak C was fit with the high-temperature tail (beyond the peak half-height on the downslope) excluded. Due to irreversibility, an accurate value for ΔC_p is unobtainable, so $\Delta\Delta G$ was calculated by two procedures: by assuming constant ΔH and ΔS and by estimating the temperature dependence of ΔH and ΔS using a value of 0.12 cal/g for ΔC_p, which is an average value for several small, globular proteins (*34*). These methods give a stabilization $\Delta\Delta G$ of 2.8−3.4 kcal/mol for transition B and 0.6−0.8 kcal/mol for transition C (Table 1).

Structure. As with native human mitochondrial MnSOD (*1*), the Q143N mutant forms a homotetramer composed of four identical subunits. The superposition of the wild-type tetramer and Q143N tetramer shows no apparent subunit displacement. Each asymmetric unit of the crystal contains two subunits that form interactions that resemble those seen in dimeric bacterial Fe and MnSODs (*1*). Each subunit fold can be divided into a N-terminal helical hairpin domain (residues 1−84) and a C-terminal α/β domain (residues 85−198). Two domains are joined by the active-site manganese ion. The Mn ion is coordinated by His 26, His 74, Asp 159, His 163, and a water molecule; the averaged coordination bond distance is 2.2 Å with trigonal bipyramidal geometry. Residue 143, glutamine in the wild type and asparagine in our mutant Q143N, is located near the active site with an Nϵ2−Mn distance of 4.6 Å in wild type and Nδ2−Mn distance of 6.3 Å in the mutant (Figure 6). Yet, the Q143 Oϵ1−Mn ion distance of 5.4 Å is surprisingly similar to the Q143N Oδ1−Mn ion distance of 5.3 Å. Two four-helix bundles form the tetrameric interface, and 2-fold symmetry places four copies of the mutated residue Asn 143 in the tetramer. Thus, any structural destabilization or stabilization resulting from the single amino acid mutation is quadrupled in the assembled tetrameric enzyme.

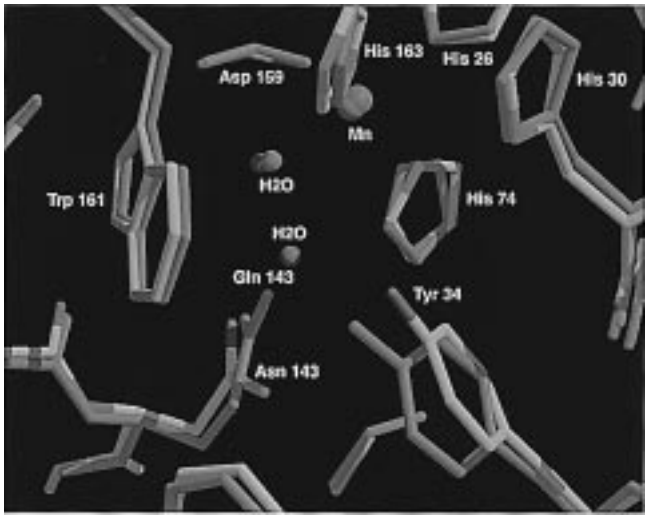

FIGURE 6: Active-site differences and similarities revealed by the least-squares superposition of Q143N human MnSOD (multicolored) and wild-type MnSOD (pink). Residues 34 and 143 are indicated. In the Q143N mutant, not only is the amide side chain of 143 more distant from the manganese ion but the position of the side chain of Tyr 34 is also changed.

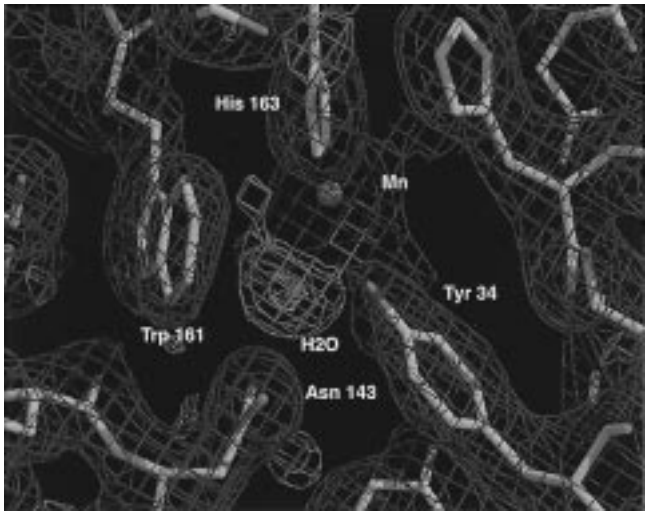

FIGURE 7: Electron density map of Q143N human MnSOD calculated with Fourier coefficients $2F_o - F_c$ (1σ blue and 8σ magenta contours), $F_o - F_c$ (2σ gray and 4σ green contours), and phases derived from the final model. A water molecule has filled the cavity left by the replacement Gln 143 → Asn and provides bridging hydrogen bonds from Asn 143 Nδ2 to the Tyr 34 side chain and to the hydroxyl/water ligand of the Mn ion.

Q143N MnSOD closely resembles the wild-type enzyme. The RMS deviation for Cα atoms when one subunit of this mutant and the wild type are superimposed is 0.36 Å, reflecting the close similarity of these structures, as shown for the active site in Figure 6. The Cα chains of residues, which connect the two subdomains, shift 0.93 and 0.47 Å for subunits A and B, respectively, when compared with the wild type. Both the position and coordination geometry of Mn are only slightly changed compared with the native structure (Figure 6). The difference Fourier electron density map ($F_{Q143N}-F_{WT}$, α_{WT}) shows negative (2σ) electron density at Gln143, indicating the removal of Cδ. Asn 143 Oδ1 maintains the hydrogen bond to Trp 123 Nϵ1 (3.2 Å) but loses the hydrogen bond to the hydroxyl or water ligand of the Mn ion, which moves about 0.3 Å toward Asp 159 Oδ2 (2.7 Å in distance). The Q143N mutant has almost identical Trp 123 and Asp 159 side-chain positions compared to wild type. A new water molecule (H_2O 33 in subunit B and H_2O 88 in subunit A) is introduced to fill the cavity left by the deletion of Gln 143 Cδ (Figure 7). In subunit A of the mutant, the Tyr 34 side chain OH is pushed away 0.9 Å (0.4 Å in subunit B) by this new water molecule and hence no longer forms a direct hydrogen bond with the side chain of Asn 143. Both Tyr 34 and Asn 143 are now hydrogen-bonded to the new water molecule, which also hydrogen-bonds to the original hydroxyl ligand (2.8 Å in distance). The differences in the Tyr 34 position between the two subunits in the crystallographic asymmetric unit indicate an increased flexibility in this region resulting from the inserted water molecule.

DISCUSSION

We made the conservative replacement Gln 143 → Asn in human MnSOD, corresponding to shortening the length of the side chain by one methylene group, which increased the distance between the amide nitrogen and the manganese by 1.7 Å, whereas the side-chain carbonyl oxygen distance only increased by 0.1 Å. Although this mutation could potentially leave a cavity in the active site, a 4σ peak near Asn 143 corresponding to a water molecule in both subunits is observed in the $F_o - F_c$ difference Fourier map of the mutant (Figure 7). This water molecule bridges Asn 143 and the hydroxyl/water molecule which is a ligand of the manganese. The hydrogen-bonding distances are 2.8 and 2.6 Å for Nδ2−H_2O and H_2O−H_2O, respectively (Figure 7). This additional water molecule in the Q143N mutant fills the cavity and thus may stabilize the mutant structure. The stabilization resulting from the Q143N mutation, which alters the active-site hydrogen bonding by inserting a new water molecule, is consistent with Gln 143 having a functional role in MnSOD activity. A comprehensive mutational analysis of functionally important residues in T4 lysozyme similarly showed that the enzyme residues involved in function are not optimized for stability (*35*).

One very significant change caused by the replacement Gln → Asn is the apparent shift of the reduction potential of manganese to a more positive value that renders Q143N MnSOD stable in the Mn(II) state under our solution conditions, while the wild-type MnSOD is clearly and predominantly in the Mn(III) state. Support for this conclusion comes first from the absence of a visible absorption spectrum of the mutant Q143N, whereas wild-type hMn(III)SOD has a broad absorbance with a maximum at 480 nm (*6*). Reduction of bacterial MnSOD to the Mn(II) state was previously observed to abolish the visible spectrum (*31*). A second result indicating the predominance of Mn(II) in the resting state of Q143N hMnSOD is the presence of a complex EPR spectrum between 1000 and 2000 G (Figure 5). Wild-type MnSOD from *E. coli* reduced to the Mn(II) state by dithionite also showed spectra with many resonances in this region; SOD containing Mn(III) is EPR-silent (*31*, *36*). However, the hyperfine splitting for the multiplet near 1000−2000 G is much better resolved for Q143N hMn(II)SOD than for either of these spectra for wild-type Mn(II)SOD from *E. coli.*

Several features in the mutant Q143N hMnSOD, such as an alteration in the hydrogen-bond scheme and ligand

distances in the mutant, could influence the reduction potential of manganese at the active site, although it is difficult to quantitate their contributions (*37*). One feature that could alter the reduction potential at the active site is the decrease in the metal−amide dipole interaction when the amide nitrogen is moved 1.7 Å more distant from the manganese in the mutant. The averaged Mn−His Nϵ2 distances for the three His ligands in Q143N mutant is 2.2 Å, which is only slightly longer than the corresponding distances in wild type (2.1 Å). The Mn−Asp Oδ1 distance for the single Asp ligand in the Q143N mutant is also slightly longer than in the wild-type (2.0 vs 1.9 Å), and so is the Mn−$H_2O(OH^-)$ distance (2.2 vs 2.1 Å). The coordination geometry expands slightly in the mutant. Although these shifts are small and within possible structural error, the observed longer coordination bond distances could reflect a charge and environment change around the Mn ion consistent with the spectroscopic evidence of a change in the reduction potential. The smaller improvement in stability of Q143N compared to Y34F (*32*) may reflect the additional water bridge that maintains the 143 to 34 side-chain hydrogen-bond linkage that apparently creates an energy cost to the folded active-site structure of Q143N and allows variation in the position of the Tyr 34 side chain. The Y34F structure by comparison has completely lost the hydrogen-bonded link to the 143 side chain (*32*). The newly introduced water bridge is remarkable for making short hydrogen bonds to Tyr 34 OH (2.5 Å) and Asn 143 Oδ1 (2.6 Å) and for packing tightly against the aromatic ring of Trp 161. All of these interactions of the new water bridge suggest possible stabilization of a H_3O^+. Another phenomenon is that in the Q143N mutant the Mn−OH distance is 2.26 Å in subunit A, a distance that is slightly longer than the typical 2.0 Å Mn−OH distance, indicating a possible $OH^- \rightarrow H_2O$ switch and consistent with the reduction potential change of the Mn ion. Taken together, the changes in Q143N, consistent in the two subunits within the crystallographic asymmetric unit, suggest the introduction of a protonated water and the possible partial shift of the hydroxyl ligand of Mn to a water molecule. Moreover, the much lower pH required for crystallization suggests that there may be some additional protons to complement the reduced Mn charge in the mutant.

Catalysis by Q143N hMnSOD showed no product inhibition even at $[O_2^{\bullet -}]/[E]$ as great as 50. Thus measurement of its catalysis was much more straightforward than with either wild-type (*6*, *12*) or Y34F hMnSOD (*32*), which become inhibited within 1 or 2 ms under our experimental conditions. The catalysis of superoxide decay by Q143N MnSOD followed simple Michaelis−Menten kinetics as shown in the typical experiment of Figure 2. Therefore, although the protein exists as a tetramer, there appears to be no cooperativity.

The replacement Gln 143 → Asn causes a decrease in the value of k_{cat}/K_m for $O_2^{\bullet -}$ decay by 3 orders of magnitude compared with the wild-type at pH 9.6 (Table 2). k_{cat}/K_m was strongly pH-dependent in the range of pH 8.5−10.5, suggesting a pK_a near or below 8.5 with a maximum near 7×10^6 M^{-1} s^{-1} (Figure 3). Thus, although both wild-type (*12*) and Y34F hMnSOD (*32*) show values of k_{cat}/K_m that are near 10^9 M^{-1} s^{-1} and are diffusion-controlled, the mutant Q143N hMnSOD exhibits catalysis that is not diffusion-controlled. It is unlikely that the replacement Gln 143 → Asn has significantly impeded the access of superoxide to the active site; rather, this mutation has changed the rate-limiting step for k_{cat}/K_m in Q143N to a step other than diffusion of superoxide. This is also consistent with the appearance of an apparent value of the pK_a of k_{cat}/K_m to a value near or below 8.5. This pK_a for k_{cat}/K_m is not observed in the wild-type hMnSOD (*6*).

Table 2: Values of the Steady-State Parameters for the Decay of Superoxide Catalyzed by Human MnSOD and Two Mutants

enzyme	k_{cat} (ms^{-1})	k_{cat}/K_m (μM^{-1} s^{-1})
wild-type MnSOD[a]	40	800
Y34F MnSOD[a]	3.3	870
Q143N MnSOD[b]	0.3	0.82

[a] Data for wild type (*6*) measured at pH 9.4 and 20 °C by pulse radiolysis and for Y34F (*32*) measured at pH 9.6 and 20 °C by pulse radiolysis. [b] Data obtained by stopped-flow spectrophotometry at pH 9.4 and 5 °C.

The cause of this apparent pK_a is not clear, but because it occurs in the rate constant k_{cat}/K_m describing catalysis at very low substrate concentration, it probably describes processes involved in the conversion of superoxide to oxygen and peroxide anion rather than rate-limiting proton transfers, which are expected near maximal velocity when the enzyme is working near full capacity. This view is strengthened by the solvent hydrogen isotope effect of unity on k_{cat}/K_m for Q143N. The ratio k_{cat}/K_m for *E. coli* FeSOD shows a similar dependence on pH with an apparent pK_a near 9.4 (*38*). This apparent pK_a is believed to be caused by the addition of a hydroxide ligand to the metal in the ferric form; the pK_a near 9 in the ferrous form is believed to be the ionization of Tyr 34 (*14*). The reduced catalytic activity of Q143N hMnSOD and the enhanced stability of the Mn(II) state are related. The reduction potentials of the Cu/Zn, Fe, and MnSODs are all in the range +0.25 V to +0.40 V to give maximum thermodynamic driving force in the oxidation and reduction cycles necessary for rapid catalysis of the disproportionation (*9*). The alteration of hMnSOD caused by the replacement Gln → Asn has most likely shifted the reduction potential to more a positive value outside of this range and compromised the catalytic efficiency of the mutant and possibly altered the pK_a of the water bound to manganese.

The catalytic turnover k_{cat} for Q143N hMnSOD is less than that of the wild type by about 2 orders of magnitude (Table 2), and there is some evidence for a weak pH dependence with an apparent pK_a near 10 (Figure 4). This rate constant represents the maximal rate of catalysis, and the solvent hydrogen isotope effect of 1.9 ± 0.2 suggests a contribution from the proton-transfer steps that protonate the peroxide anion at the active site and allow rapid dissociation of product (Scheme 1). The altered positions of Tyr 34 and Asn 143 may impair the proton transfer to the active site, resulting in a reduced value of k_{cat}. Of course, the altered pK_a of the manganese-bound water, suggested by both our structural and kinetic results, could also affect the proton-transfer rate.

Azide binding to superoxide dismutase offers clues to the binding of superoxide itself. In bacterial MnSOD, azide is a ligand of the metal and hydrogen-bonded to the hydroxyl of the Tyr 34 side chain (*14*). With these hydrogen-bonding residues repositioned in Q143N, we can expect the binding of substrate to be altered in Q143N hMnSOD. This is

Scheme 1

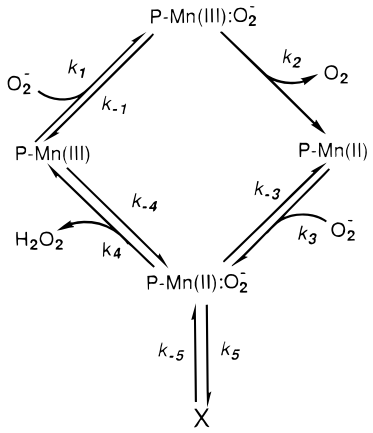

Table 3: Values of the Rate Constants for Catalysis by Wild-Type and Q143N Human Manganese Superoxide Dismutase[a]

rate constant	wild-type MnSOD[b]	Q143N MnSOD[c]
k_1 (M^{-1} s^{-1})	2×10^9	2×10^9
k_{-1} (s^{-1})	2×10^4	1.5×10^6
k_2 (s^{-1})	8×10^4	600
k_3 (M^{-1} s^{-1})	2×10^9	2×10^9
k_{-3} (s^{-1})	2×10^4	1.5×10^6
k_4 (s^{-1})	8×10^4	600
k_{-4} (M^{-1} s^{-1})	3×10^2	1×10^3
k_5 (s^{-1})	2×10^4	2×10^4
k_{-5} (s^{-1})	130	200

[a] Obtained by fitting the model of Scheme 1 using KINSIM (*39*) to the data for catalysis of the decay of superoxide. [b] Fit was to pulse radiolysis data measured at 20 °C and pH 9.4 (*6*). [c] Fit was to stopped-flow data measured at 5 °C and pH 9.4 under the conditions of Figure 3.

consistent with the following observations based on Scheme 1, which is a mechanism used to describe catalysis by wild-type MnSOD (*6*, *12*). The fit of Scheme 1 shows increased off rates of substrate (k_{-1}, k_{-3}) for Q143N compared with those in wild type (Table 3). The results of Table 3 may not represent unique solutions to the appropriate kinetic equations for hMnSOD and mutants; however, they qualitatively represent trends in the catalytic pathway between wild-type and mutants of hMnSOD.

It is also possible that Gln 143 in wild-type MnSOD contributes to tight binding of product peroxide and that in Q143N MnSOD an interaction responsible for that binding is missing, thus decreasing product inhibition in this mutant. However, there is a second explanation for the lack of product inhibition in this mutant; that is, the overall rate constant for peroxide formation at the active site may be much less than the rate constant for dissociation of peroxide from the enzyme. This suggestion is consistent with a fit of the kinetic data for Q143N hMnSOD to Scheme 1 (Table 3), showing that catalysis by Q143N MnSOD can be explained using rate constants for the formation of the dead-end complex (k_5, k_{-5}) that are the same as for the wild-type enzyme. That is, even though there is no evidence from these data of product inhibition in catalysis by Q143N hMnSOD, this is not necessarily due to a weaker binding affinity of the inhibiting form of peroxide at the active site.

Conclusions. (1) Glutamine 143 has a predominant role in maintaining the catalytic efficiency in MnSOD. (2) The replacement Gln 143 → Asn moves the side chain amide nitrogen 1.7 Å more distant from the manganese in Q143N, and due to this shift and the altered position of Tyr 34 in the mutant, the hydrogen bond between these two residues can no longer be maintained in Q143N. (3) The mutant Q143N showed no product inhibition when compared with the wild type, which appears to be inhibited by product peroxide. (4) Gln 143 in MnSOD has a substantial role in maintaining a reduction potential favorable for the oxidation and reduction cycles in the catalytic disproportionation of superoxide. With this residue replaced by Asn, the Michaelis parameters for catalysis are significantly compromised by 2−3 orders of magnitude. (5) Catalysis by Q143N MnSOD obeys simple Michaelis kinetics, showing that this variant does not exhibit cooperativity in catalysis. (6) A solvent hydrogen isotope effect on k_{cat} for Q143N hMnSOD suggests that the pathway for maximal velocity contains rate-contributing proton transfers to form product hydroperoxide anion or hydrogen peroxide. The replacement Gln 143 → Asn alters the hydrogen-bonding scheme in the active site and creates a new bound water site. These changes may affect the delivery of protons to product peroxide. (7) Catalysis by neither the wild-type nor the Q143N variant of MnSOD studied here are susceptible to enhancement by up to 100 mM concentrations of certain buffers in solution.

ACKNOWLEDGMENT

We are grateful to Dr. Don O'Connor for his assistance with pulse radiolysis and to Dr. Cecilia Ramilo and Amy Hearn for their help in preparation of enzyme. We thank Professors Marian Stankovich and George Reed for their very helpful comments and guidance. We thank Dr. Christopher Bruns for critically reviewing the draft, Dr. Elizabeth Getzoff and Dr. Terence Lo for many discussions and suggestions, and Sudip Parikh and Andrew S. Arvai for their help on data collections.

REFERENCES

1. Borgstahl, G. E. O., Parge, H. E., Hickey, M. J., Beyer, W. F., Hallewell, R. A., and Tainer, J. A. (1992) *Cell 71*, 107−118.
2. Wagner, U. G., Pattridge, K. A., Ludwig, M. L., Stallings, W. C., Werber, M. M., Oefner, C., Frolow, F., and Sussman, J. L. (1993) *Protein Sci. 2*, 814−825.
3. Parker, M. W., and Blake, C. C. F. (1988) *J. Mol. Biol. 199*, 649−661.
4. Ludwig, M. L., Metzger, A. L., Pattridge, K. A., and Stallings, W. C. (1991) *J. Mol. Biol. 219*, 335−358.
5. Stoddard, B. L., Ringe, D., and Petsko, G. A. (1990) *Protein Eng. 4*, 113−119.
6. Hsu, J.-L., Hsieh, Y., Tu, C. K., O'Connor, D., Nick, H. S., and Silverman, D. N. (1996) *J. Biol. Chem. 271*, 17687−17691.
7. McCord, J. M., Boyle, J. A., Bay, E. D., Rizzolo, L. J., and Salin, M. L. (1977) in *Superoxide and Superoxide Dismutase* (Michelson, A. M., McCord, J. M., and Fridovich, I., Eds.) pp 129−138, Academic Press, London.
8. Getzoff, E. D., Cabelli, D. E., Fisher, C. L., Parge, H. E., Viezzoli, M. S., Banci, L., and Hallewell, R. A. (1992) *Nature 358*, 347−351.
9. Holm, R. H., Kenepohl, P., and Solomon, E. I. (1996) *Chem. Rev. 96*, 2239−2314.
10. McAdam, M. E., Fox, R. A., Lavelle, F., and Fielden, E. M. (1977) *Biochem. J. 165*, 71−79.
11. McAdam, M. E., Lavelle, F., Fox, R. A., and Fielden, E. M. (1977) *Biochem. J. 165*, 81−97.

12. Bull, C., Niederhoffer, E. C., Yoshida, T., and Fee, J. A. (1991) *J. Am. Chem. Soc. 113*, 4069−4076.
13. Smith, M. W., and Doolittle, R. F. (1992) *J. Mol. Evol. 34*, 175−184.
14. Lah, M. S., Dixon, M. M., Pattridge, K. A., Stallings, W. C., Fee, J. A., and Ludwig, M. L. (1995) *Biochemistry 34*, 1646−1660.
15. Beck, Y., Oren, R., Amit, B., Levanon, A., Gorecki, M., and Hartman, J. R. (1987) *Nucleic Acids Res. 15*, 9076.
16. Beck, B. A., Bartfield, D., Yavin, Z., Levanon, A., Gorecki, M., and Hartman, J. R. (1988) *Bio/Technology 6*, 930−935.
17. Otwinowski, Z., and Minor, W. (1997) in *Methods in Enzymology* (Carter, C. W., Jr., and Sweet, R. M., Eds.) Vol. 276, pp 307−326, Academic Press, New York.
18. McRee, D. E. (1992) *J. Mol. Graphics 10*, 44−47.
19. Brünger, A. T., Kuriyan, J., and Karplus, M. (1987) *Science 235*, 458−460.
20. Jiang, J.-S., and Brünger, A. T. (1994) *J. Mol. Biol. 243*, 100−115.
21. Read, R. J. (1986) *Acta Crystallogr. A42*, 140−149.
22. Ramachandran, G. N., and Sasisekharan, V. (1968) *Adv. Protein Chem. 23*, 283−438.
23. Bernstein, F. C., Koetzle, T. F., Williams, G. J. B., Meyer, E. F., Brice, M. D., Rodgers, J. R., Kennard, O., Shimanouchi, T., and Tasumi, M. (1977) *J. Mol. Biol. 112*, 535−542.
24. Borgstahl, G. E. O., Parge, H. E., Hickey, M. J., Beyer, W. F., Hallewell, R. A., and Tainer, J. A. (1996) *Biochemistry 35*, 4287−4297.
25. Sturtevant, J. M. (1987) *Annu. Rev. Phys. Chem. 38*, 463−488.
26. Schwarz, H. A. (1981) *J. Chem. Educ. 58*, 101−105.
27. Rabani, J. and Nielson, S. O. (1969) *J. Phys. Chem. 73*, 3736−3744.
28. McClune, G. J. and Fee, J. A. (1978) *Biophys. J. 24*, 65−69.
29. Valentine, J. S. and Curtis, A. B. (1975) *J. Am. Chem. Soc. 97*, 224−226.
30. Leatherbarrow, R. J. (1987) Enzfitter: a nonlinear regression data analysis program for the IBM PC, Elsevier Biosoft, Cambridge, England.
31. Fee, J. A., Shapiro, E. R., and Moss, T. H. (1976) *J. Biol. Chem. 251*, 6157−6159.
32. Guan, Y., Hickey, M. J., Borgstahl, G. E. O., Hallewell, R. A., Lepock, J. R., O'Connor, D., Hsieh, Y., Nick, H. S., Silverman, D. N., and Tainer, J. A. (1998) *Biochemistry 37*, 4722−4730.
33. Lepock, J. R., Ritchie, K. P., Kolios, M. C., Rodahl, A. M., Heinz, K., and Kruuv, J. (1992) *Biochemistry 31*, 12706−12712.
34. Privalov, P. L., and Khechinashvili, N. N. (1974) *J. Mol. Biol. 86*, 665−684.
35. Shoichet, B. K., Baase, W. A., Kuroki, R., and Matthews, B. W. (1995) *Proc. Natl. Acad. Sci. U.S.A. 92*, 452−456.
36. Whittaker, J. W., and Whittaker, M. M. (1991) *J. Am. Chem. Soc. 113*, 5528−5540.
37. Stephens, P. J., Jollie, D. R., and Warshel, A. (1996) *Chem. Rev. 96*, 2491−2513.
38. Bull, C. and Fee, J. A. (1985) *J. Am. Chem. Soc. 107*, 3295−3304.
39. Barshop, B. A., Wrenn, R. F., and Frieden, C. (1983) *Anal. Biochem. 130*, 134−145.

BI972395D